Forward inclusive production spectrum of K_S, Λ^0, $\bar{\Lambda}^0$, and n in the collision of 200-GeV/c π^-, K^-, $\bar{p}$, and p on Be

R. T. Edwards,* T. Devlin, B. Edelman,† and L. Schachinger
Rutgers, The State University, New Brunswick, New Jersey

G. Bunce,‡ R. Handler, P. Martin,§ L. Pondrom, and M. Sheaff
University of Wisconsin, Madison, Wisconsin

P. T. Cox, K. Heller, O. Overseth, and P. Skubic¶
University of Michigan, Ann Arbor, Michigan

R. Grobel,‖ U. Nauenberg, and K. Wild
University of Colorado, Boulder, Colorado

(Received 3 February 1978)

We have measured the forward production spectra of various neutral particles produced by π^-, K^-, $\bar{p}$, and p at 200 GeV/c, and by π^- at 290 GeV/c incident on a Be target. The salient features of these measurements are (1) copious production of K_S^0 at large Feynman x_L for incident π^- and K^-, (2) production of roughly equal fluxes of Λ^0 and $\bar{\Lambda}^0$ for incident π^-, and (3) close similarity of the following spectra: $\pi^- \to n$ and $K^- \to \Lambda^0$; $\pi^- \to \Lambda^0$, $\pi^- \to \bar{\Lambda}^0$, and $p \to K_S^0$; $\pi^- \to K_S^0$ and $p \to \Lambda^0$. The overall features of the various distributions seem to agree with the ideas of dimensional counting presented in the constituent-interchange model of quark collisions. Results are presented in terms of the invariant cross section $Ed^3\sigma(x_L, P_T = 0)/dp^3$ per Be nucleus for each inclusive reaction.

INTRODUCTION

We present here the results of an experiment carried out at the Fermi National Accelerator Laboratory. This experiment measured the yield of K_S^0, Λ^0, $\bar{\Lambda}^0$, n, or $\bar{n}$ in the forward direction. The incident particles were π^-, K^-, $\bar{p}$, and p and the target was Be. The data presented is for 200 GeV/c incident momentum, and, in the case of π^- incident, also for 290 GeV/c. In the text that follows we denote the various reactions as $a \to c$ where we imply $a + \mathrm{Be} \to c + X$.

We describe the apparatus in Sec. I where we discuss in particular the calorimeter used to measure the neutron spectrum. In Sec. II we discuss the various facets of the data collection and analysis, and in Sec. III the results and the comparison with a model.

I. THE DETECTOR

Much of the apparatus has already been described.[1] It was located in the Fermilab M2 line where the beam struck a 30-cm-long beryllium target 6 mm in diameter (Fig. 1). The observed neutral particles traversed a collimator in a 22-kG field 5.5 m long. The narrowest point of the collimator was a hole 4 mm in diameter, 3.3 m from the target, centered at 0° from the charged beam. The largest observed production angle was 1.5 mrad, while the average angle of neutral particles that made it through the collimator was 0.7 mrad. The parts of the detector that measured the K_S, Λ^0, and $\bar{\Lambda}^0$ decays consisted of a veto counter, V, followed by a decay vacuum pipe, D. Next was a spectrometer consisting of the multiwire proportional chambers (MWPC) 1, 2, 3; followed by a superconducting momentum-analyzing magnet M, and by the MWPC's 4, 5, 6. In addition, 12- and 6-mm-diameter scintillator counters, B1 and B2, were placed just before the target.

New to this detector were the beam Cherenkov counters C1, C2 upstream of the target, and the calorimeter C placed at the end of the spec-

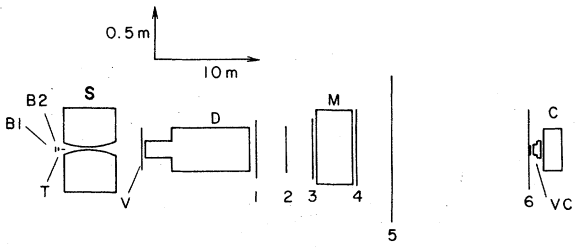

FIG. 1. Elevation view of the spectrometer. B1 and B2 are beam scintillators, T is the beryllium target, S is the magnetized shield, V is a veto counter to define the evacuated decay region, D; 1, 2, 3, M, 4, 5, 6, form the multiwire proportional chamber magnetic spectrometer. C is the calorimeter shown in detail in Fig. 2.

trometer. The Cherenkov counters were helium filled differential counters, each with a parabolic mirror to focus the light onto two separate photomultipliers. One photomultiplier (PM) detected the light emitted at small angles, while the other was set to observe the larger-angle light. During the 200-GeV/c run, C2 was set to detect light emitted by kaons in the small-angle PM, and light emitted by pions in the large-angle PM. C1 was set to detect the light emitted by protons in the small-angle PM, and light emitted by pions or kaons in the large-angle PM. The pressure settings for C1 and C2 were 208 and 180 mm of Hg, respectively.

The other new part of the detector was the calorimeter, C, used to determine the neutron spectrum. It consisted of a segmented lead-glass array with dimensions 37.5 cm wide, 50 cm high, and 150 cm deep. There were 73 blocks each 10×10 cm$^2\times37.5$ cm, each placed with its length transverse to the neutral beam, and viewed end on by a single 5-cm-diameter photomultiplier. Preceding this array was a conventional iron-scintillator sandwich. In front there were four iron plates 15×15 cm^2 in cross section, followed by 13 plates 20×20 cm^2 for a total of 17 plates each 2.5 cm thick. The plates were separated by six scintillation counters as shown in Fig. 2. In addition, the first element of the calorimeter was a 12.5-cm lead-glass block, γ, used to separate γ's from hadrons. A small veto counter (VC) was placed in front of the calorimeter to ensure that only neutral particles triggered the calorimeter. The 42.5 cm of iron and 162.5 cm of lead glass gave a total of approximately 8 interaction lengths of material in the calorimeter.

The calorimeter had a total of 80 photomultipliers each with its own analog-to-digital converter. The pulse heights were initially set equal. The final relative calibrations used in the analysis were determined by allowing 100-, 200-, and 290-GeV/c beam particles to strike the calorimeter.

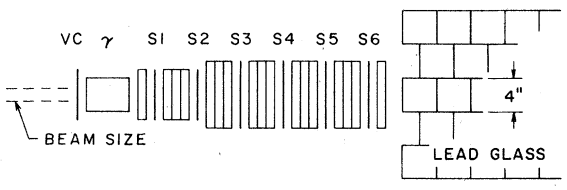

FIG. 2. Side view of the calorimeter used to measure the $n/\bar{n}$ spectra. The composition is described in the text. S1 through S6 are scintillators separating iron sheets. The lead-glass array was placed at the far end of the iron scintillator "precalorimeter." The initial lead-glass block γ helped identify γ rays in the beam for γ-hadron discrimination.

The calibration was carried out in the following manner: We define the quantity

$$E=\sum_{i=1}^{80} c_i P_i ,$$

where c_i are the relative calibration constants desired and P_i are the pulse heights in the various phototubes which result when the beam of known energy E_b strikes the calorimeter. We minimize $\chi^2=\sum(E-E_b)^2$ by solving the 80 simultaneous linear equations,

$$\frac{d}{dc_i}\sum_{\text{events}}\left(E_b-\sum_{i=1}^{80} c_i P_i\right)^2=0 .$$

This method of calibrating a segmented calorimeter turned out to be very simple and efficient. One-thousand beam particles were sufficient to carry out such calibration of the calorimeter. This number of particles could be obtained with just three machine pulses. This approach to calibration avoids laborious documentation of the gains of the individual tubes, and establishes the relative weights to be given to the various sections of the calorimeter. This calibration was carried out twice during the run which lasted only one week. No significant variations were observed in the resolution or in the calibration constants. The RMS resolution of the calorimeter was 10% at 200 GeV/c and 14% at 100 GeV/c. The calorimeter was linear to 2% in this range. This resolution is shown in Fig. 3.

II. DATA COLLECTION AND ANALYSIS

An incident beam particle was defined by the coincidence between B1 and B2 and the appropriate combination of Cherenkov PM pulses that defined the mass of particles. For example, a pion was defined by the coincidence (C2 large-angle PM) · (B1) · (B2) and no count in (C2 small-angle PM). The four possible Cherenkov pulses in

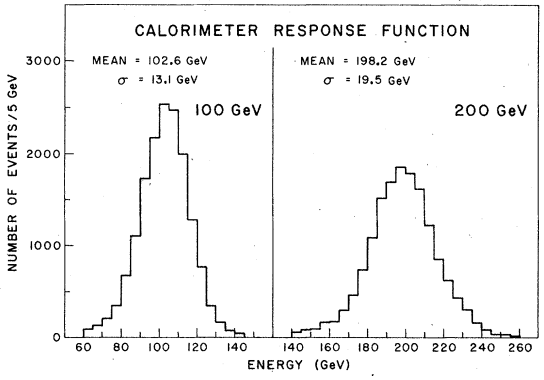

FIG. 3. Energy resolution of the calorimeter to 100- and 200-GeV/c negative hadrons.

coincidence with B1 and B2 were recorded and the identity of the beam particle was determined off line during the analysis stage. Most combinations of the various signals of C1 and C2 in coincidence with B1 · B2 were summed during the data collecting. These sums were used to normalize the cross sections presented in Sec. III. In the negative 200-GeV/c beam the ratios K^-/π^- and $\bar{p}/\pi^-$ were 3.1% and 0.7% respectively. In the positive beam the large proton flux made it difficult to tag the π^+ and K^+ in the beam. Hence, we only present the data for protons incident. The small π^+ and K^+ contamination in the beam was removed by means of the Cherenkov counters.

An event was written on tape if there was no count in the veto V, a coincidence B1 · B2 · MWPC 1 · 2 · 3 · 4 and a count in each side of MWPC 5. The yield of neutral V's (K^0_S, Λ^0, and $\bar{\Lambda}^0$) was the number of observed events divided by the acceptance of the apparatus for detecting an event in a given momentum bin. This detection efficiency, shown in Fig. 4, was determined using Monte Carlo techniques. The computer program included lifetime losses, geometrical limitations due to detector sizes, chamber inefficiency, chamber spatial resolution, and multiple scattering of the charged tracks. In addition we corrected for the finite beam and target size. Finally, the Monte Carlo generated events were reconstructed by the data-analysis program to include in the efficiency any losses due to reconstruction failures. Further corrections were made for misidentification of decay type, target out rate, and absorption of the produced particles in the target and other matter in the beam line. The corrections for accidentals varied from 5% for incident pions to 30% for incident antiprotons. In Fig. 5 we show the calculated resolution of the spectrometer compared with the data. The agreement is adequate for the cuts necessary in the analysis of this experiment.

Three target lengths (30, 15, and 7.5 cm) were used to study two effects. First, they were used to determine any change in the shape of the momentum spectrum which might occur because of second-order interactions in the target. No change in the shape of the momentum spectrum was observed. Second, the different target lengths were used to measure the absorption of incoming

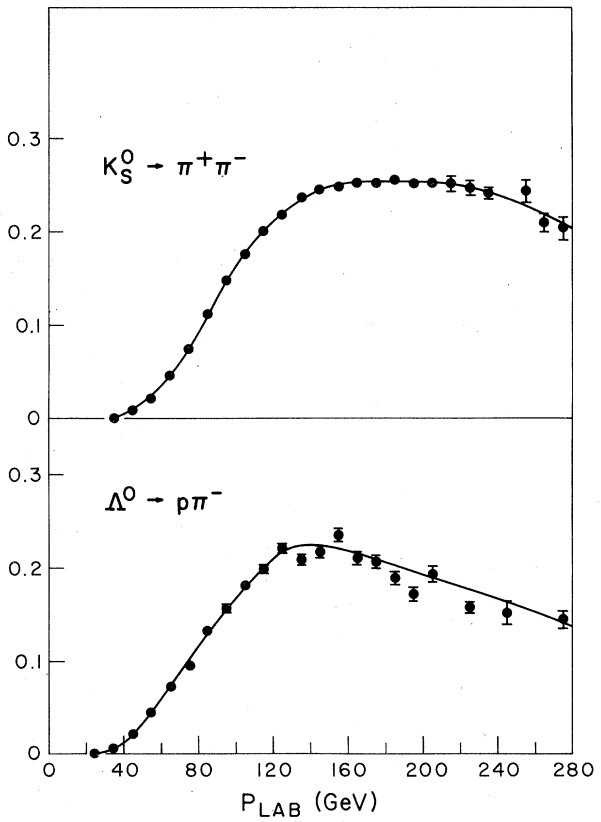

FIG. 4. Monte Carlo results for the overall detection efficiency for decays via the charge mode of K^0_S and Λ^0 produced at the Be target as a function of laboratory momentum. The cutoff at low momentum is mainly due to attenuation in the 5.5-mm-long neutral collimator. The geometrical acceptance of the spectrometer itself for Λ^0's which decayed within the evacuated decay path was about 90%.

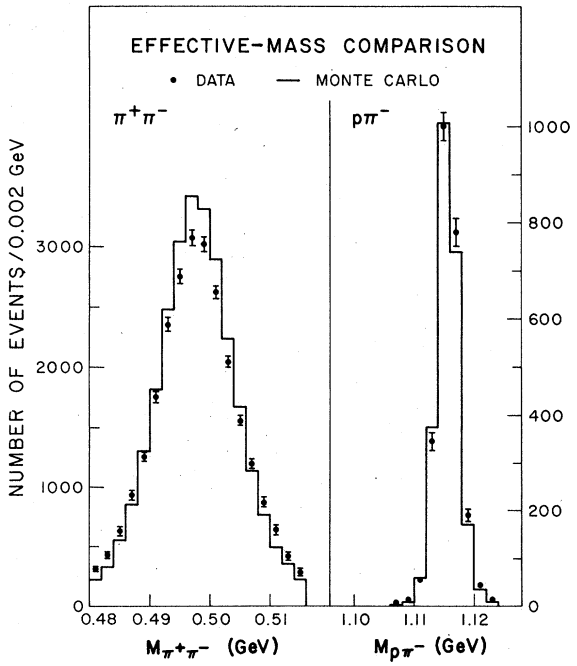

FIG. 5. Invariant-mass distributions for $K^0_S \to \pi^+\pi^-$ and $\Lambda^0 \to p\pi^-$ compared to Monte Carlo calculations, demonstrating that the measurement errors in spatial reconstruction are well understood.

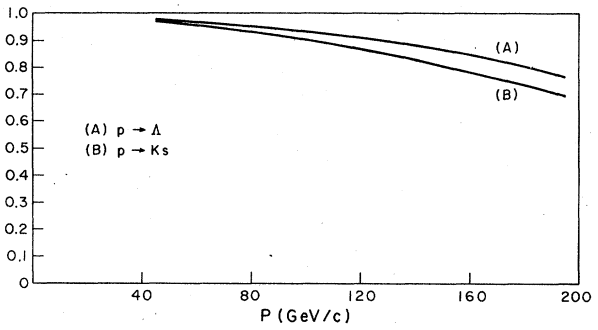

FIG. 6. Factors by which the observed yields should be divided to correct for the finite width of the acceptance in the transverse momentum derived from the data of Ref. 2, where the transverse-momentum dependence of the reactions $p \to \Lambda^0$ and $p \to K_S^0$ where measured. The average between these two correction factors was used in the present experiment as discussed in the text.

and outgoing particles. The correction for the absorption of incoming and produced particles in the target lead to a normalization of the observed flux by a factor of 1.62 with an overall uncertainty of 20% [full width at half maximum (FWHM)]. The relative-normalization uncertainty of different particle types was 15% (FWHM).

A number of cuts were applied to the neutral decay data, most important of which are the combined mass cuts and target pointing cuts. Cuts were applied to the reconstructed masses of K^0's, Λ^0's, and $\bar{\Lambda}^0$'s at 2.2σ, where σ is the mass uncertainty which varied from event to event and is calculated from the error matrix of the fit to a V of the chamber hits in the spectrometer. Since the Monte Carlo–produced events had a mass dis-

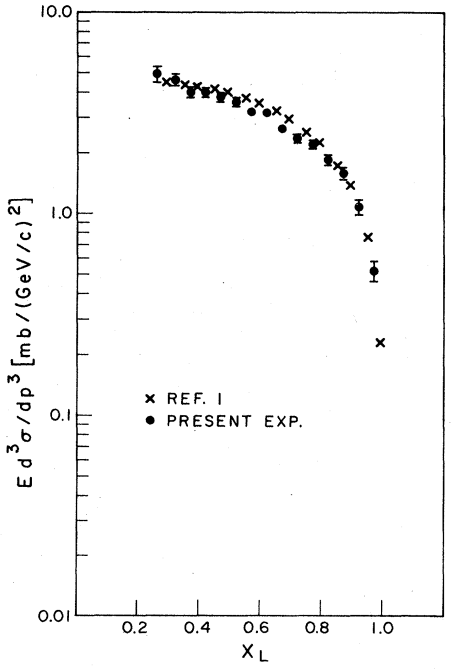

FIG. 7. Comparison of the 300-GeV/c spectrum of Ref. 2 and the 200-GeV/c spectrum of the present experiment, plotted as the invariant cross section versus x_L.

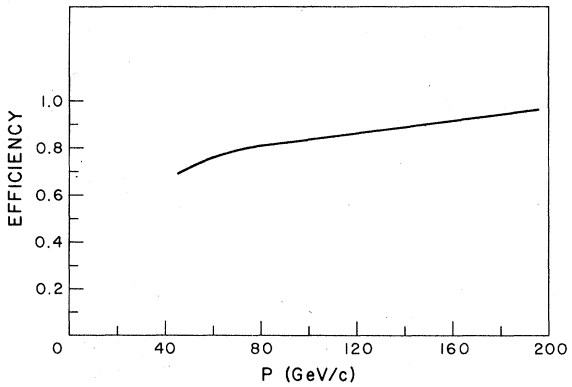

FIG. 8. Detection efficiency for hadrons in the calorimeter, including loss due to cuts made in the longitudinal development of the shower to eliminate γ rays from the sample.

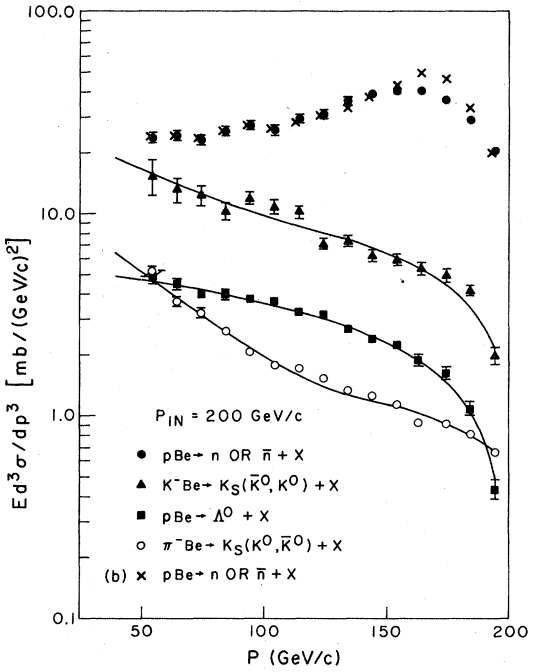

FIG. 9. Invariant cross sections, at $P_T = 0$ and 200 GeV/c, $K^- \to K_S^0$, $p \to \Lambda^0$, and $\pi^- \to K_S^0$ vs laboratory momentum. Each of these reactions has $n(a\bar{c}) = 2$ according to the quark-counting rules. The points ×, labeled (b) in the list, are "unfolded," such that when convoluted with the resolution function, give the closed circles, the observed shape for $p \to n$. The solid curves represent the best fits shown in Table IV.

TABLE I. Invariant cross section $E\,d^3\sigma/dp^3$ in mb/(GeV/c)^2 for the inclusive reactions at 200 GeV/c incident momentum.

P (GeV/c)	x_L	$\pi^- \to K_S + X$	$\pi^- \to \Lambda + X$	$\pi^- \to \bar{\Lambda} + X$	$\pi^- \to n, \bar{n} + X$
55	0.27	5.2 ± 0.3	1.35 ± 0.12	0.79 ± 0.09	3.9 ± 0.5
65	0.32	3.69 ± 0.18	1.00 ± 0.07	0.61 ± 0.06	3.8 ± 0.3
75	0.37	3.25 ± 0.12	0.71 ± 0.05	0.53 ± 0.04	2.7 ± 0.2
85	0.42	2.61 ± 0.08	0.47 ± 0.03	0.46 ± 0.03	2.27 ± 0.20
95	0.47	2.09 ± 0.06	0.33 ± 0.02	0.267 ± 0.021	2.15 ± 0.17
105	0.52	1.79 ± 0.05	0.264 ± 0.017	0.197 ± 0.015	1.62 ± 0.14
115	0.57	1.72 ± 0.04	0.186 ± 0.013	0.112 ± 0.011	1.12 ± 0.12
125	0.62	1.55 ± 0.04	0.131 ± 0.011	0.101 ± 0.009	0.90 ± 0.11
135	0.67	1.33 ± 0.03	0.096 ± 0.009	0.071 ± 0.008	0.71 ± 0.09
145	0.72	1.27 ± 0.04	0.063 ± 0.007	0.043 ± 0.006	0.37 ± 0.08
155	0.77	1.14 ± 0.04	0.036 ± 0.005	0.030 ± 0.005	0.25 ± 0.07
165	0.82	0.93 ± 0.02	0.017 ± 0.004	0.015 ± 0.004	0.18 ± 0.06
175	0.87	0.92 ± 0.02	0.010 ± 0.002	0.0053 ± 0.0020	0.16 ± 0.06
185	0.92	0.82 ± 0.02	0.0056 ± 0.0020	0.0035 ± 0.0016	0.02 ± 0.05
195	0.97	0.67 ± 0.02	0.0030 ± 0.0015	0.0015 ± 0.0011	0.01 ± 0.04

P (GeV/c)	x_L	$K^- \to K_S + X$	$K^- \to \Lambda + X$	$K^- \to \bar{\Lambda} + X$	$K^- \to n, \bar{n} + X$
55	0.27	15.3 ± 3.1	3.2 ± 1.1	0.4 ± 0.4	5 ± 4
65	0.32	13.1 ± 1.8	1.8 ± 0.6	0.6 ± 0.3	2 ± 3
75	0.37	12.4 ± 1.4	3.3 ± 0.6	0.8 ± 0.3	3 ± 2
85	0.42	10.3 ± 0.9	2.5 ± 0.4	0.23 ± 0.14	2.6 ± 1.7
95	0.47	12.0 ± 0.8	2.0 ± 0.3	0.22 ± 0.11	1.6 ± 1.8
105	0.52	10.9 ± 0.8	1.4 ± 0.2	0.16 ± 0.08	-0.6 ± 1.4
115	0.57	10.2 ± 0.7	0.69 ± 0.15	0.14 ± 0.07	-1.8 ± 1.3
125	0.62	7.2 ± 0.4	0.77 ± 0.16	0.12 ± 0.07	-0.4 ± 1.0
135	0.67	7.4 ± 0.4	0.47 ± 0.11	0.09 ± 0.06	0.0 ± 1.0
145	0.72	6.3 ± 0.4	0.49 ± 0.12	0.06 ± 0.04	0.3 ± 0.9
155	0.77	6.0 ± 0.4	0.30 ± 0.08	0.02 ± 0.02	-0.5 ± 0.7
165	0.82	5.4 ± 0.4	0.18 ± 0.07	0.02 ± 0.02	-0.2 ± 0.7
175	0.87	5.0 ± 0.4	0.20 ± 0.08	<0.02	0.1 ± 0.6
185	0.92	4.2 ± 0.2	0.16 ± 0.06	<0.02	0.2 ± 0.5
195	0.97	2.0 ± 0.2	0.50 ± 0.04	<0.02	0.0 ± 0.4

P (GeV/c)	x_L	$p \to K_S + X$	$p \to \Lambda + X$	$p \to \bar{\Lambda} + X$	$p \to n, \bar{n} + X$
55	0.26	2.3 ± 0.4	4.9 ± 0.4	0.36 ± 0.10	23.7 ± 1.5
65	0.32	2.0 ± 0.2	4.5 ± 0.3	0.11 ± 0.04	24.4 ± 1.3
75	0.37	1.32 ± 0.14	4.0 ± 0.2	0.09 ± 0.03	23.2 ± 1.2
85	0.42	1.00 ± 0.09	3.99 ± 0.18	0.014 ± 0.009	25.7 ± 1.2
95	0.47	0.67 ± 0.06	3.80 ± 0.15	0.043 ± 0.014	27.4 ± 1.2
105	0.52	0.49 ± 0.04	3.65 ± 0.13	0.015 ± 0.008	28.1 ± 1.1
115	0.57	0.34 ± 0.03	3.26 ± 0.12	0.010 ± 0.006	29.7 ± 1.1
125	0.62	0.24 ± 0.02	3.21 ± 0.11	0.006 ± 0.004	31.3 ± 1.0
135	0.67	0.143 ± 0.019	2.68 ± 0.10	0.002 ± 0.002	36.4 ± 1.1
145	0.72	0.099 ± 0.016	2.41 ± 0.09	<0.002	39.0 ± 1.0
155	0.77	0.056 ± 0.012	2.26 ± 0.10	<0.002	40.2 ± 1.1
165	0.82	0.008 ± 0.005	1.90 ± 0.11	<0.002	40.9 ± 1.1
175	0.87	0.005 ± 0.002	1.64 ± 0.11	<0.002	37.1 ± 1.0
185	0.92	0.0020 ± 0.0020	1.10 ± 0.09	<0.002	29.2 ± 0.9
195	0.97	<0.002	0.54 ± 0.05	<0.002	20.3 ± 0.7
205					12.0 ± 0.5
215					5.2 ± 0.4

TABLE I. (continued)

P (GeV/c)	x_L	$\bar{p} \to K_S + X$	$\bar{p} \to \bar{\Lambda} + X$	$\bar{p} \to \bar{n}, n + X$
55	0.26	0 ± 7	<9	27 ± 8
65	0.32	8 ± 5	1.8 ± 1.9	24 ± 7
75	0.37	1.6 ± 1.5	3.3 ± 2.0	24 ± 6
85	0.42	0.9 ± 0.9	1.6 ± 1.0	29 ± 6
95	0.47	0.6 ± 0.6	4.9 ± 1.6	26 ± 5
105	0.52	<0.4	4.6 ± 1.4	37 ± 6
115	0.57	1.2 ± 0.7	5.0 ± 1.3	26 ± 6
125	0.62	1.4 ± 0.7	4.5 ± 1.2	34 ± 6
135	0.67	0.6 ± 0.5	1.6 ± 0.7	40 ± 6
145	0.72	0.3 ± 0.3	2.8 ± 0.8	41 ± 6
155	0.77	<0.2	2.5 ± 0.8	48 ± 6
165	0.82	0.2 ± 0.2	3.3 ± 0.8	48 ± 6
175	0.87	0.2 ± 0.2	2.4 ± 0.8	35 ± 5
185	0.92	<0.2	1.4 ± 0.6	34 ± 5
195	0.97	<0.2	0.7 ± 0.4	18 ± 3
205				11 ± 3
215				5 ± 2

tribution very nearly the same as the data, Fig. 5, the same cuts were applied to the Monte Carlo acceptance program, thus correcting for losses in the tails of the distributions. The other major cut applied required that the neutral-V momentum vector point back to the target within a radial distance of 8 mm. Any events that occurred outside this limit were removed from the data and Monte Carlo events. A Λ^0 or K^0 which does not come from the target most often comes from a beam particle striking air after passing through the target, or , as in the case of $p \to \Lambda$, from

TABLE II. Invariant cross section $E\, d^3\sigma/dp^3$ in mb/(GeV/c)^2 for the inclusive reactions at 290 GeV/c incident momentum.

P (GeV/c)	x_L	$\pi^- \to K_S + X$	$\pi^- \to \Lambda + X$	$\pi^- \to \bar{\Lambda} + X$	$\pi^- \to n + X$
55	0.18	10 ± 2	1.8 ± 0.7	1.8 ± 0.7	4 ± 3
65	0.21	7.7 ± 1.2	2.3 ± 0.6	1.7 ± 0.5	6.6 ± 1.8
75	0.25	7.8 ± 0.9	1.8 ± 0.4	1.3 ± 0.3	5.4 ± 1.5
85	0.28	6.4 ± 0.6	0.9 ± 0.2	1.3 ± 0.3	4.4 ± 1.2
95	0.32	4.1 ± 0.4	0.73 ± 0.17	0.85 ± 0.10	6.4 ± 1.0
105	0.35	3.6 ± 0.3	0.53 ± 0.13	0.59 ± 0.13	3.9 ± 0.8
115	0.38	3.0 ± 0.3	0.73 ± 0.14	0.20 ± 0.08	4.8 ± 0.8
125	0.42	2.9 ± 0.2	0.42 ± 0.10	0.47 ± 0.11	3.9 ± 0.8
135	0.45	2.30 ± 0.22	0.38 ± 0.09	0.23 ± 0.07	3.2 ± 0.7
145	0.48	2.26 ± 0.20	0.31 ± 0.08	0.36 ± 0.09	1.8 ± 0.6
155	0.52	1.70 ± 0.17	0.23 ± 0.07	0.15 ± 0.06	2.6 ± 0.4
165	0.55	1.93 ± 0.17	0.21 ± 0.06	0.15 ± 0.06	1.0 ± 0.3
175	0.58	1.88 ± 0.18	0.18 ± 0.06	0.14 ± 0.05	0.9 ± 0.4
185	0.62	1.77 ± 0.17	0.12 ± 0.05	0.04 ± 0.02	0.6 ± 0.4
195	0.65	1.36 ± 0.15	0.11 ± 0.05	0.11 ± 0.05	0.6 ± 0.2
205	0.68	1.50 ± 0.16	0.05 ± 0.04	0.08 ± 0.04	0.4 ± 0.2
215	0.72	1.31 ± 0.14	0.08 ± 0.04	0.08 ± 0.04	0.17 ± 0.24
225	0.75	1.27 ± 0.14	0.05 ± 0.03	<0.018	0.10 ± 0.22
235	0.78	0.99 ± 0.12	<0.018	0.035 ± 0.026	0.16 ± 0.22
245	0.82	1.07 ± 0.12	0.035 ± 0.025	<0.018	0.21 ± 0.21
255	0.85	0.65 ± 0.10	0.017 ± 0.017	<0.018	0.19 ± 0.19
265	0.88	0.89 ± 0.12	0.016 ± 0.017	<0.018	0.06 ± 0.16
275	0.92	0.71 ± 0.11	0.017 ± 0.017	<0.018	-0.02 ± 0.14
285	0.95	0.47 ± 0.08	<0.017	<0.018	-0.10 ± 0.11
295	0.98				

neutrons produced by the protons which produce Λ's in the narrow opening of the collimator. After these cuts were made, the radial-distance distribution of the Monte Carlo events and the real events agreed very well.

One final correction that has to be applied to all the data is a yield renormalization due to the finite size of the beam and the finite solid angle subtended by the collimator. To determine this correction we need to know the transverse-momentum dependence of the reactions being measured. Such a measurement was not carried out and hence in principle this correction cannot be carried out. To indicate the magnitude of the correction we calculated the factor that the measured fluxes must be divided by to determine the differential cross section at $P_T = 0$. This was carried out for the reaction $p \to \Lambda$ and $p \to K_S$ where the P_T dependence has been measured.[2] This factor is shown in Fig. 6. We assume that all the reactions we measured have a similar P_T dependence and hence a similar correction. We have applied the average between the two corrections shown in Fig. 6 to the measured yields and the resultant differential cross section is shown in the tables and figures discussed in the next section.

Our yield for $p \to \Lambda$ at 200 GeV/c was compared with the same yield measured in another experi-

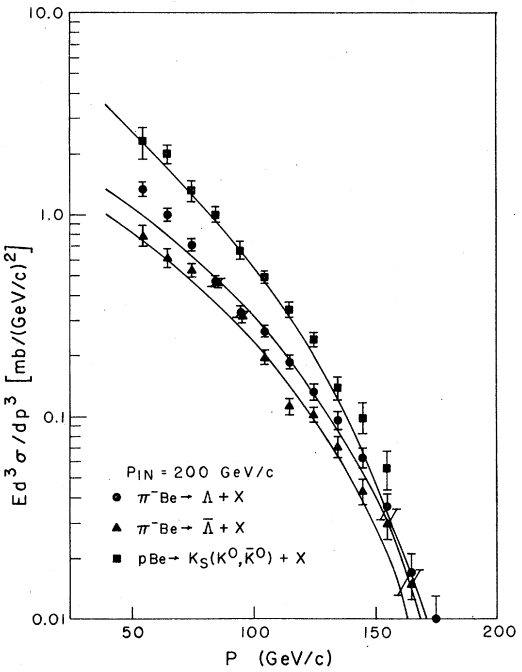

FIG. 11. Invariant cross sections at $P_T = 0$ and 200 GeV/c for $\pi^- \to \Lambda^0$, $\pi^- \to \bar{\Lambda}^0$, and $p \to K_S^0$ vs laboratory momentum. These reactions also have $n(a\bar{c}) = 3$. The solid curves represent the best fits shown in Table IV.

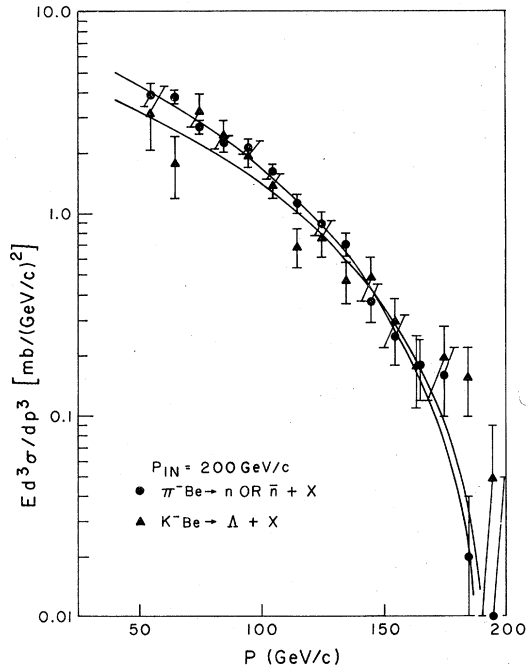

FIG. 10. Invariant cross sections at $P_T = 0$ at 200 GeV/c, for $\pi^- \to n$, $K^- \to \Lambda^0$ vs laboratory momentum. These reactions have $n(a\bar{c}) = 3$. The solid curves represent the best fits shown in Table IV.

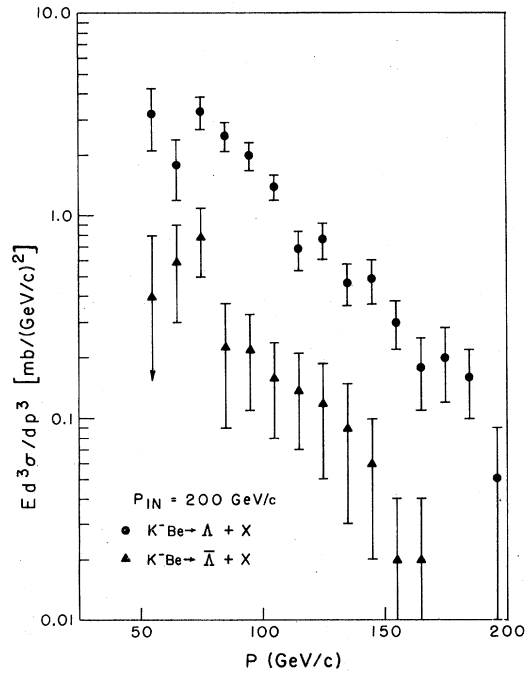

FIG. 12. Invariant cross sections at $P_T = 0$ and 200 GeV/c for $K^- \to \Lambda^0$ and $K^- \to \bar{\Lambda}^0$ vs laboratory momentum. These reactions also have $n(a\bar{c}) = 3$.

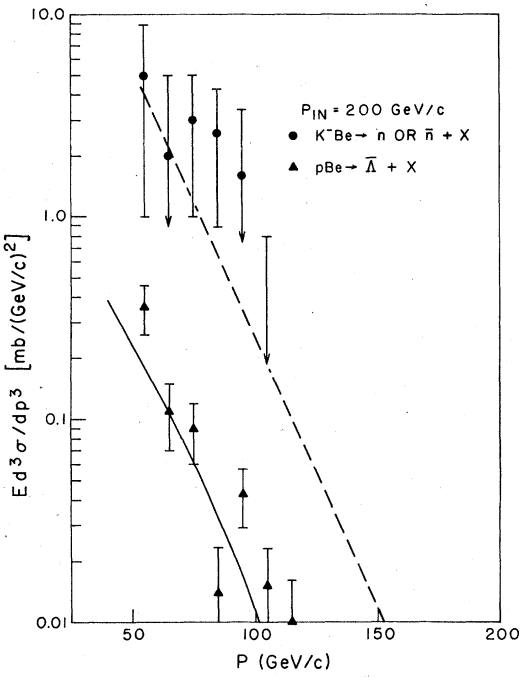

FIG. 13. Invariant cross sections at $P_T = 0$ and 200 GeV/c for $K^- \rightarrow n/\bar{n}$, for which $n(a,\bar{c}) = 5$, and for $p \rightarrow \bar{\Lambda}^0$, for which $n(a,\bar{c}) = 6$. The dashed line is to guide the eye. The solid curve represents the best fit shown in Table IV.

ment[2] at 300 GeV/c. The comparison of the two experiments is shown in Fig. 7. The agreement between the two experiments, normalized independently with completely different techniques, is good.

In the case of a calorimeter run an event was written on tape if there was no count in VC, a coincidence between B1, B2, and γ or B1, B2, S5, and S6, and no count in γ (Fig. 2). We studied the pattern of energy deposition of the shower in the various elements of the calorimeter to separate the hadrons from γ's. This study led to very efficient cuts that removed γ's from hadrons. Some hadrons were lost as a result of these cuts. The hadron efficiency was determined by observing charged beam particles in the calorimeter. This hadron detection efficiency is show in Fig. 8.

The neutron (antineutron[3]) yield was determined by subtracting from the hadron yield measured in the calorimeter, the K_L yield expected at the calorimeter. The K_L yield was calculated from the observed K_S flux and the spectrometer detection efficiency. The number of Λ^0, $\bar{\Lambda}^0$, and K_S reaching the calorimeter was negligible.

The effect of the calorimeter energy resolution was minimal for $\pi^- \rightarrow n$ and $K^- \rightarrow n$. In both cases the K_L yield which was subtracted from the hadron yield was convoluted by the measured functional shape of the resolution at 200 GeV/c The remaining neutron yield after K_L subtraction is of such a functional form that it is virtually unchanged by the resolution. Therefore no correction has been made. The yields $p \rightarrow n$, $\bar{p} \rightarrow \bar{n}$, however, are considerably affected by the calorimeter resolution because of the rapid variation of the distribution above Feynman $x_L \approx 0.6$ ($x_L = P_L/p_{L\,max}$). In order to determine the true distribution one needs to convolute the calorimeter's energy-resolution function to a prospective, theoretically deduced, energy distribution and compare the resulting distribution with the data. In reality we do not know *a priori* what the theoretical distribution is and hence it cannot be determined in an unambiguous manner. However, to illustrate the effect of the resolution, the curve labeled (b) in Fig. 9 when folded with the experimental resolution function gives the observed $p \rightarrow n$ spectrum. The data presented in the tables have not been corrected for resolution.

III. RESULTS

The inclusive cross sections in the forward direction are shown in terms of the invariant cross section $Ed^3\sigma/dp^3$. The results[4] are presented in

TABLE III. Parameters predicted by the CIM model to describe the various inclusive differential cross sections.

Reaction	$n(a\,\bar{c})$	$g(c/a)$	F
(1) $p \rightarrow n$	2	3	1
(2) $K^- \rightarrow \bar{K}^0$	2	3	1
(3) $p \rightarrow \Lambda$	2	3	1
(4) $\pi^- \rightarrow K^0$	2	3	1
(5) $\pi^- \rightarrow n$	3	5	3
(6) $K^- \rightarrow \Lambda$	3	5	3
(7) $\pi^- \rightarrow \Lambda$	3	5	3
(8) $\pi^- \rightarrow \bar{\Lambda}$	3	5	3
(9) $p \rightarrow K^0$	3	5	3
(10) $K^- \rightarrow \bar{\Lambda}$	3	5	3
(11) $\pi^- \rightarrow \bar{K}^0$	4	7	5
(12) $K^- \rightarrow K^0$	4	7	5
(13) $K^- \rightarrow n$	5	9	7
(14) $p \rightarrow \bar{K}^0$	5	9	7
(15) $p \rightarrow \bar{\Lambda}$	6	11	9

TABLE IV. Results of a χ^2 fit to the various inclusive differential cross sections measured using the CIM-model parametrization: $E(d^3\sigma/dp^3) = R(1-x_L)^F\,[1+d(1-x_L)^4]$.

Reaction	F (CIM model)	NSQ[a]	R	F	d	DF	χ^2/DF
(1) $p \to \Lambda$	1	Yes	5.75 ± 0.12	0.6555 ± 0.013	0	13	0.7
(2) $K^- \to K_S$	1, 5	No ($\bar{K}^0$), Yes (K^0)	12.8 ± 0.3	0.50 ± 0.03	1.6 ± 0.5	12	2.2
(3) $\pi^- \to K_S$	1, 5	Yes (K^0), Yes ($\bar{K}^0$)	1.60 ± 0.05	0.262 ± 0.013	7.9 ± 0.6	12	3.5
(4) $\pi^- \to n$ or $\bar{n}$	3	No	8.4 ± 0.6	2.3 ± 0.1	0	13	0.64
(5) $K^- \to \Lambda$	3	No	5.8 ± 1.1	2.02 ± 0.20	0	13	1.8
(6) $\pi \to \Lambda$	3	Yes	2.58 ± 0.30	3.01 ± 0.09	0	13	3.2
(7) $\pi \to \bar{\Lambda}$	3	Yes	1.98 ± 0.16	3.05 ± 0.11	0	13	2.5
(8) $p \to K_S$	3, 7	Yes (K^0), Yes ($\bar{K}^0$)	5.6 ± 0.8	3.4 ± 0.2	0.8 ± 0.7	12	0.7
(9) $p \to \bar{\Lambda}$	9	Yes	$2.2^{+1.8}_{-1.6}$	$7.6^{+1.7}_{-2.4}$	0	7	2.1

[a]Needs strange quark or antiquark from the sea of quarks antiquarks to produce the final state.

Tables I and II and in Figs. 9–13.

We discuss the qualitative behavior of these cross sections in terms of the constituent-interchange model (CIM).[5] We carry out fits to the data using a most simplified interpretation of this model, not only because of the difficulty in using the full version, but also because the simplified version shows with greatest clarity some striking regularities in the data. In the CIM model the inclusive reactions are described as the sum of many terms of the form (for $P_T = 0$)

$$E\frac{d^3\sigma}{dp^3} = R(1-x_L)^F . \tag{1}$$

We will only consider the leading-order term where the parameter F is $g(c/a) - 2$ and $g(c/a) \equiv 2n(a\bar{c}) - 1$. The quantity $n(a\bar{c})$ represents the net number of valence quarks in the $a\bar{c}$ state where a refers to the incident particle and c to the outgoing particle. As an example, in the inclusive process $\pi^- \to \Lambda^0$, the π^- valence-quark content is $\bar{u}\,d$ while for the Λ^0 it is $u\,ds$. The number $n(a\bar{c})$ is then $\bar{u}+d+\bar{d}+\bar{s}+\bar{u}$. The counting is done so that quark-antiquark pairs such as $d+\bar{d}$ are not counted. Hence, $n(a\bar{c})$ is 3 in this case. Predicted values of $n(a\bar{c})$, $g(c/a)$, and F are given for the various reactions in Table III.

In Table IV we present the values of the parameters describing the differential cross section. These fits were obtained using a χ^2-minimizing program. We observe a striking qualitative correlation between the value of F in the fits and the CIM-model parameter $g(c/a)$ namely $F \approx g(c/a) - 2$. This is in agreement with the simplified model presented in the previous paragraph. In Fig. 14 we present the values of F versus the parameter $g(c/a)$. The line drawn is the simplified CIM prediction $F = g(c/a) - 2$.

Some additional comments are in order. The model does not include the effects due to the complex nuclear target. Reference 2 discusses these effects on the x distribution by comparing spectra from Be, Cu, and Pb targets. Expressed in terms of $(1-x)^F$, the exponent F, for the reaction $p \to \Lambda$, increases from 0.65 for Be to 0.72 for Pb. Such a small change implies a negligible effect in the comparison of Be and H induced reactions. The errors presented are purely statistical and do not include the errors introduced by our lack of know-

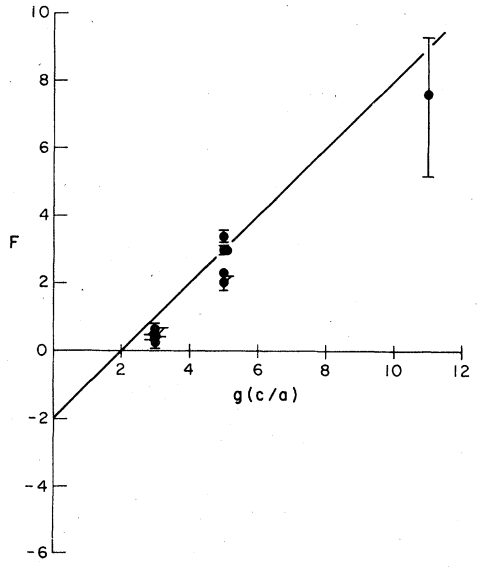

FIG. 14. Comparison of the fitted values of the power F in the parametrization $Ed^3\sigma/dp^3 = R(1-x_L)^F$ to the predictions of the constituent-interchange model. The straight line is the prediction $F = g(c/a) - 2$, where $g(c/a) = 2n(a,\bar{c}) - 1$, and $n(a,\bar{c})$ is the number of valence quarks in the reactions as listed in Table III.

ledge in the corrections applied to the data. The comparison of the present data to Eqs. (1) and (2) is qualitative, as indicated by the poor χ^2 fits in some cases. Reactions 2, 3, and 8 in Table IV have to be analyzed in terms of two final states; namely, K^0 and $\bar{K}^0$. We introduce the additional state by adding a nonzero parameter d, as follows:

$$E\frac{d^3\sigma}{dp^3} = R(1-x_L)^F[1+d(1-x_L)^4]. \quad (2)$$

These three reactions were the only cases where d was allowed to vary from zero. The effect of d can be seen most clearly in Fig. 9 for the reaction $\pi^- \to K_S$. The sudden large change in the slope of the cross section at $p = 100$ GeV/c represents the $\bar{K}^0$ production being observed for $p < 100$ GeV/c. The cross section for $p > 100$ GeV/c would be due mostly to K^0 production. Surprising in this fit would be the large $\bar{K}^0$ rate expected at low values of x_L for incident π^-. Also it is observed that the value of R for those reactions where a strange quark or antiquark has to be pulled out of the sea is smaller than the other reactions, in some cases by a factor of ~2.

A very interesting test of these ideas would be to study the x_L dependence of the production of K^+, K^-, K^0, and $\bar{K}^0$ for incident π^- and π^+. This model would predict that for incident π^+ there would be more K^+ than K^- at large x_L but more $\bar{K}^0$ than K^0 at large x_L. In the case of incident π^- the situation would be the opposite.

ACKNOWLEDGMENTS

One of us (U.N.) would like to thank Professor R. Blankenbecler for his many discussions of the theory. We would like to thank the staff of Fermilab and special thanks to the meson area for their help during the time this data was being obtained. This research was supported by the Department of Energy and the National Science Foundation.

---

*Present address: Bell Laboratories, Holmdel, New Jersey.
†Present address: Ford Motor Company, Allen Park, Michigan.
‡Present address: Brookhaven National Laboratories, Upton, New York.
§Present address: Lawrence Berkeley Labs, Berkeley, California.
¶Present address: Rutgers University, New Brunswick, New Jersey.
||Present address: University of Wisconsin, Madison, Wisconsin.

[1]G. Bunce *et al.*, Phys. Rev. Lett. 36, 1113 (1976); P. Skubic *et al.*, Michigan-Wisconsin-Rutgers Report No. COO-881-22 (unpublished); P. Skubic, thesis, Univ. of Michigan, 1977, Report No. UM HE 77-32 (unpublished).
[2]K. Heller *et al.*, Phys. Rev. D 16, 2737 (1977). See also Ref. 1 above.
[3]The calorimeter cannot distinguish between neutrons and antineutrons. Hence all the yields represent the sum of these two states.
[4]In the tables, a number preceded by the symbol < implies that no events occurred in that bin and we present the upper limit based on one event.
[5]R. Blankenbecler and S. J. Brodsky, Phys. Rev. D 10, 2973 (1974); S. J. Brodsky and G. R. Farrar, Phys. Rev. Lett. 31, 1153 (1973). References to other work can be found in these articles.